Membrane insertion mechanism of the caveola coat protein Cavin1

Kang-Cheng Liu[a], Hudson Pace[a,b,c], Elin Larsson[a], Shakhawath Hossain[d] (ID), Aleksei Kabedev[d] (ID), Ankita Shukla[a] (ID), Vanessa Jerschabek[e], Jagan Mohan[a,1], Christel A. S. Bergström[d], Marta Bally[b,c] (ID), Christian Schwieger[e] (ID), Madlen Hubert[a,d,2] (ID), and Richard Lundmark[a,2] (ID)

Caveolae are small plasma membrane invaginations, important for control of membrane tension, signaling cascades, and lipid sorting. The caveola coat protein Cavin1 is essential for shaping such high curvature membrane structures. Yet, a mechanistic understanding of how Cavin1 assembles at the membrane interface is lacking. Here, we used model membranes combined with biophysical dissection and computational modeling to show that Cavin1 inserts into membranes. We establish that initial phosphatidylinositol (4, 5) bisphosphate [PI(4,5)P$_2$]–dependent membrane adsorption of the trimeric helical region 1 (HR1) of Cavin1 mediates the subsequent partial separation and membrane insertion of the individual helices. Insertion kinetics of HR1 is further enhanced by the presence of flanking negatively charged disordered regions, which was found important for the coassembly of Cavin1 with Caveolin1 in living cells. We propose that this intricate mechanism potentiates membrane curvature generation and facilitates dynamic rounds of assembly and disassembly of Cavin1 at the membrane.

caveolae | Cavin1 | membrane curvature | membrane-shaping protein | protein–lipid interactions

The typical small bulb-shaped invaginations of the plasma membrane termed "caveolae" are found in most vertebrate cells. They are highly abundant in adipocytes, muscle, and endothelial cells and are important for various physiological processes like regulation of membrane tension, lipid metabolism, and cellular signaling (1, 2). Lack or dysfunction of caveolae is connected to severe human diseases such as muscular dystrophy, cardiomyopathy, and lipodystrophy. Caveolae formation is dependent on membrane lipid composition and the coat components Caveolin1 (CAV1) and Cavin1 (3). Caveolae are enriched in cholesterol and sphingolipids (1, 2), which not only accumulate in caveolae but are actively sequestered (4). The negatively charged lipids phosphatidylserine (PS) and phosphatidylinositol (4, 5) bisphosphate [PI(4,5)P$_2$] are also enriched in caveolae (5). Lipid mapping in cells showed that both CAV1 and Cavin1 recruit specific lipid species to caveolae, hereby acting synergistically to generate the unique lipid nanoenvironment of caveolae (6, 7). CAV1 and Cavin1 are universal structural elements, and knockout of either of these proteins leads to loss of caveolae (1, 2). Electron microscopy studies on caveolae have revealed a striated protein coat lining, which is believed to comprise CAV1 and the cavin proteins (8, 9). CAV1 belongs to a family of integral membrane proteins (CAV1 to 3), where both the N and C termini protrude into the cytoplasm. CAV1 has been shown to form high-order 8S oligomers in membranes following cholesterol binding (10). Cavin1 belongs to a family composed of four different proteins (Cavin1 to 4), which exhibit tissue-specific expression patterns (3). The cavin proteins are thought to assemble with CAV1 8S complexes to form 60S and 80S complexes building up the caveola coat (11). Importantly, Cavin1 is required for membrane invagination of caveolae (12). Cryoelectron microscopy studies of such complexes proposed an architecture composed of an inner cage of polygonal units of caveolins and an outer cavin coat (13, 14). The models propose that cavin arranges into a web-like architecture composed of an interbranched trimeric complex (13) or alternatively that the cavins are stacked in rod-like trimers (14). However, it is still not understood how the unique striped or spiral pattern of the caveola coat is assembled and what intermolecular forces join the molecular components together.

The cavin proteins share a common pattern in their domain structure, containing negatively charged disordered regions (DRs) interspersed with positively charged helical regions (HRs) (Fig. 1A). The crystal structures of HR1 (Protein Data Bank [PDB] ID codes 4QKV and 4QKW) revealed an extended α-helical trimeric coiled-coil structure (15). The HR1 domain has been shown to mediate trimeric homooligomerization of Cavin1 and formation of heterocomplexes with either Cavin2 or Cavin3 in solution (15, 16). HR2 is also thought to build up a trimeric coiled coil, but this structural arrangement is dependent on HR1. In vitro studies have shown that Cavin1 binds both PI(4,5)P$_2$ and PS (15, 17). The positively charged amino acids (Lys115, Arg117,

Significance

Caveolae are cholesterol-enriched membrane invaginations linked to severe muscle and lipid disorders. Their formation is dependent on assembly of the protein Cavin1 at the lipid membrane interface driving membrane curvature. In this work, we dissect the mechanism for how Cavin1 binds and inserts into membranes using a combination of biochemical and biophysical characterization as well as computational modeling. The proposed model for membrane assembly potentiates dynamic switching between shielded and exposed hydrophobic helices used for membrane insertion and clarifies how Cavin1 can drive membrane curvature and the formation of caveolae.
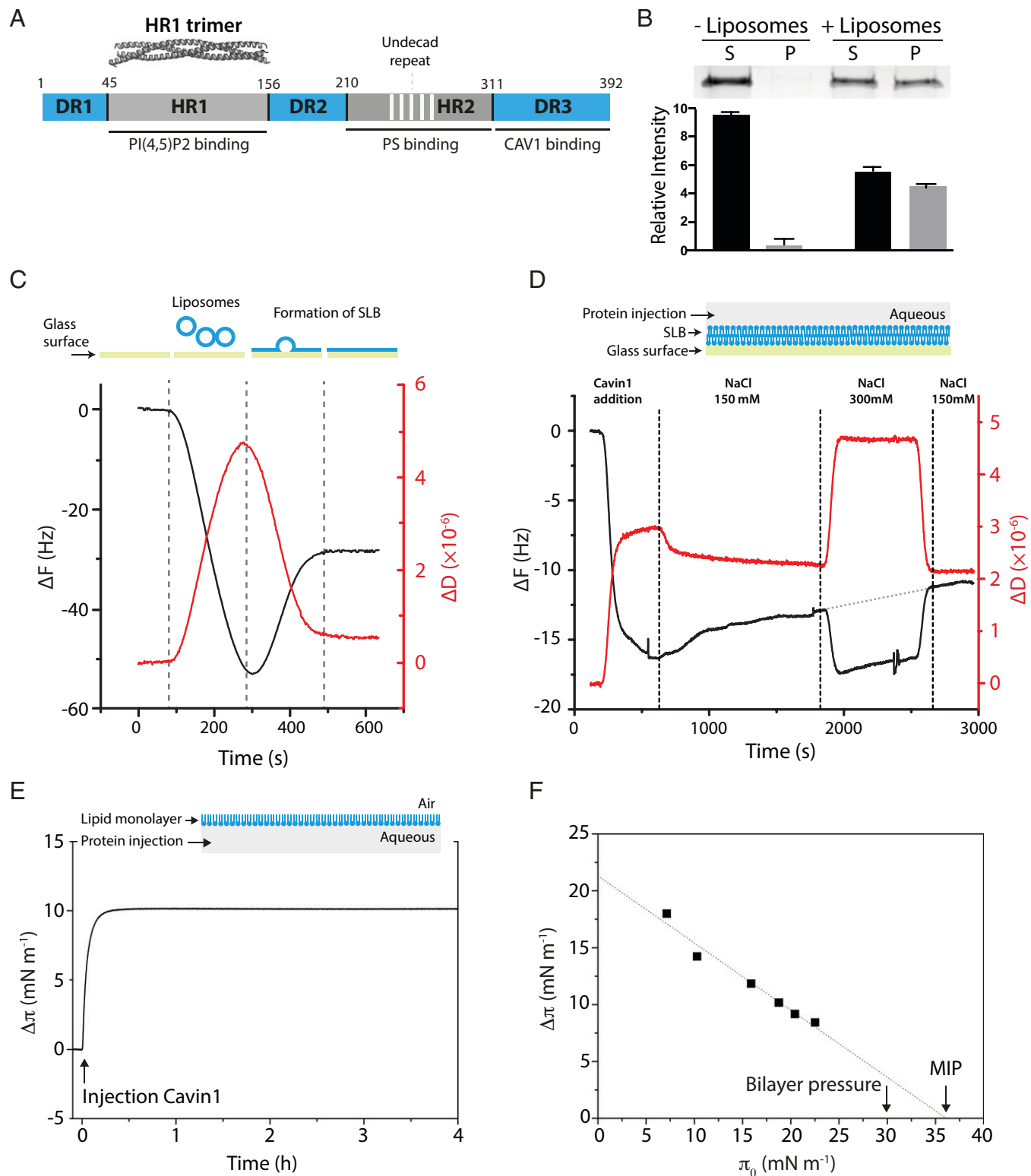
Fig. 1. Cavin1 binding and insertion into model lipid membranes. (*A*) Scheme of the domain structure of Cavin1 with DRs and HRs. White stripes mark undecad repeats. The crystal structure of HR1 (PDB ID code 4QKV) is displayed (*Top*). Regions involved in binding to PI(4,5)P$_2$, PS, and CAV1 are indicated. (*B*) Liposome cosedimentation of Cavin1. Cavin1 was incubated with or without DOPC:DOPE:PI(4,5)P$_2$ liposomes and centrifuged, and supernatant (S) and pellet (P) fractions were analyzed by SDS-PAGE. Band intensities were quantified and data are shown as mean ± SEM (*n* = 3). (*C, Top*) Scheme of SLB formation. (*C, Bottom*) QCM-D measurement showing a shift in frequency (Δ*F*) (black line) and dissipation (Δ*D*) (red line) upon SLB formation. (*D, Top*) Illustration of QCM-D setup. (*D, Bottom*) QCM-D monitoring of Cavin1 adsorption to an SLB. The responses in Δ*F* and Δ*D* correspond to Cavin1 injection and buffer rinses as indicated. The gray dotted line shows extrapolation of protein desorption from the first rinse (150 mM NaCl). (*E, Top*) Scheme of monolayer protein adsorption experiments. (*E, Bottom*) Cavin1 adsorption to DOPC:DOPE:PI(4,5)P$_2$ monolayers. Cavin1 was injected underneath the film at π_0 = 20 mN·m^{-1} and Δπ was recorded over time. (*F*) Cavin1 adsorption to lipid monolayers was measured at different π_0. The MIP value was determined by extrapolation of the Δπ/π_0 plot to the x axis.

Lys118, Lys124, Arg127) in the HR1 domain mediate specific binding to PI(4,5)P$_2$ (15), whereas a repeated sequence of 11 amino acids of the HR2 domain, identified as an undecad repeat (UC1), was shown to bind PS (17). Furthermore, Cavin1 has been shown to generate membrane curvature in vitro (15). Both HRs and DRs were required for this, and it

was proposed that Cavin1 drives membrane curvature by molecular crowding via weak electrostatic interactions between the DRs and HRs (18). Interestingly, the assembly of both CAV1 and Cavin1 was found to be dependent on the acyl chain composition of PS, suggesting that Cavin1 might also interact with the hydrophobic region of the membrane (6). Membrane insertion of Cavin1 could contribute to membrane curvature generation and the formation of caveolae. Yet, based on the current structural understanding, it is not clear how Cavin1 orients and assembles at the membrane interface.

In this work, we address the detailed mechanism by which Cavin1 binds and assembles at the lipid interface using model membranes in combination with a variety of biophysical techniques. We found that Cavin1 inserted into the membrane via the HR1 domain in a PI(4,5)P$_2$-mediated process. Membrane insertion involved partial separation of the helices in the HR1 domains in a process aided by the DR domains.

Results

Cavin1 Inserts into the Membrane, Providing Stable Membrane Association. To characterize the mechanism of membrane-driven assembly of Cavin1, we purified full-length Cavin1 from mammalian human embryonic kidney (HEK) cells (*SI Appendix,* Fig. S1 *A* and *B*). Analysis of binding to liposomes composed of DOPC:DOPE:PI(4,5)P$_2$ (55:45:5 mol%) using a cosedimentation assay showed that Cavin1 bound to membranes (*Materials and Methods* and Fig. 1*B*). To further address the membrane association in a system where binding over time could be quantified, we generated flat supported lipid bilayers (SLBs) composed of POPC:PI(4,5)P$_2$ (95:5 mol%) on a glass surface. Quartz crystal microbalance with dissipation monitoring (QCM-D) has been used extensively to monitor SLB formation (19), as it provides a distinct signature of changes in the adsorbed mass (frequency, ΔF) and stiffness (dissipation, ΔD) of the surface (Fig. 1*C*). Addition of purified Cavin1 to the SLB resulted in a steep decrease in frequency and a concerted increase in dissipation, representing adsorption of the protein to the SLB (Fig. 1*D*). When the system was rinsed with buffer (150 mM NaCl), we noticed a slow but steady release of Cavin1 from the SLB surface, indicating that the binding is at least partially reversible. We next tested if Cavin1 was adsorbed to the SLB through electrostatic interactions by treating the system with increased salt concentration. The change to buffer containing 300 mM NaCl caused a sudden protein-independent shift in both the frequency and dissipation due to the difference in viscosities between the two buffers, but was reversed upon switching back to the initial buffer (*SI Appendix,* Fig. S1*C*). We found that a higher concentration of salt did not cause additional protein desorption from the SLB beyond the slow rate observed prior to the high-salt treatment (Fig. 1*D*, gray dotted line). This suggested that, once bound to the membrane, Cavin1 was not solely interacting with the SLB through electrostatic interactions. In contrast, increased salt concentration during adsorption of Cavin1 to the SLBs led to an ~30% reduction in the amount of protein that bound (*SI Appendix,* Fig. S1*D*), thereby indicating that electrostatic interactions are important for the initial recruitment of Cavin1 to the membrane.

To determine if Cavin1 inserts into membranes, we used a Langmuir trough. This technique monitors the adsorption of a protein to a lipid monolayer suspended at an air–water interface through changes in the lateral pressure of the monolayer, thereby indicating the degree with which a protein is inserting into the monolayer (20). The surface pressure (π) is directly related to the lateral cohesion of molecules, and initial surface

pressure (π_0) values are related to the lateral packing density of the lipids before protein interactions. We prepared lipid films of DOPC:DOPE:PI(4,5)P$_2$ (55:45:5 mol%) on a buffer surface and injected Cavin1 underneath the lipid monolayer into the subphase (Fig. 1*E*). The rapid increase in surface pressure seen following protein injection indicated that Cavin1 instantly adsorbed to and inserted into the lipid monolayer (Fig. 1*E*). To get further insights into binding mechanisms, we measured Cavin1 adsorption at various π_0 and monitored surface pressure variation ($\Delta\pi$) induced by protein–lipid interaction (*SI Appendix,* Fig. S1*E*). Linear regressions of $\Delta\pi = f(\pi_0)$ provide a synergy factor (a) that corresponds to the slope +1 and describes the protein affinity for the lipid monolayer (Fig. 1*F*). The positive synergy factor value of $a = 0.41$ for Cavin1 indicated the existence of strong protein–lipid interactions (21, 22). This is further supported by a high maximum insertion pressure (MIP) value of 36.1 ± 1.9 mN·m^{-1} obtained by extrapolation of the adsorption data to the x axis (Fig. 1*F*). Proteins with MIP values above the estimated monolayer–bilayer equivalence pressure (~30 mN·m^{-1}) are considered to be well-incorporated into the lipid layer (22–24). Our data indicated a high extent of Cavin1 membrane insertion, likely due to a combination of both electrostatic and hydrophobic forces.

The N-Terminal Region of Cavin1 Adsorbs and Inserts into Membranes in a PI(4,5)P$_2$-Dependent Manner. To identify the region required for membrane insertion of Cavin1, we expressed and purified the N-terminal part (residues 1 to 190) and the C-terminal part (residues 191 to 392) of Cavin1 as recombinant proteins from bacteria (*SI Appendix,* Fig. S2*A*). By performing a cosedimentation assay, we found that the truncated Cavin1 (1–190) variant bound membranes equally well as the full-length protein (Figs. 2*A* and 1*B*, respectively). However, as previously shown, the C-terminal region (residues 191 to 392) was unable to bind to liposomes composed of DOPC:DOPE:PI(4,5)P$_2$ (17). To test whether the 1–190 region of Cavin1 was sufficient for membrane insertion, we performed adsorption experiments using lipid monolayers. The data revealed a remarkable increase in surface pressure following injection of Cavin1 (1–190) underneath a DOPC:DOPE:PI(4,5)P$_2$ film, showing that this part of the protein does indeed insert (Fig. 2*B*). While the synergy factor of $a = 0.43$ was similar to that of the full-length protein ($a = 0.41$), the MIP was determined to be 49.6 ± 2.2 mN·m^{-1} in comparison with 36.1 ± 1.9 mN·m^{-1} for full-length Cavin1, confirming that Cavin1 (1–190) has a high affinity for the lipid interface and is strongly incorporated into the monolayer (Fig. 2*C* and *SI Appendix,* Fig. S2*B*).

To investigate the effect of protein insertion on membrane organization, we used infrared reflection–absorption spectroscopy (IRRAS). IRRA spectra of the pure lipid films consisting of either DOPC:DOPE:PI(4,5)P$_2$ (Fig. 2*D*) or DOPC:DOPE (*SI Appendix,* Fig. S2*C*) displayed characteristic C=O vibrational bands at ~1,730 cm^{-1} originating from the ester group of the lipids. After injection of Cavin1 (1–190), the presence of the protein at the air–buffer interface was indicated by the amide I′ band with a maximum at ~1,640 cm^{-1} (Fig. 2*D* and *SI Appendix,* Fig. S2*C*). The intensity of amide I′, which correlates to the amount of adsorbed protein, was increased when PI(4,5)P$_2$ was present in the lipid layer. To assess the amount of inserted protein per lipid molecule, the ratios of integral intensities of amide I′/ν(C=O) of various IRRA spectra recorded at different angles of incidence were calculated for both lipid monolayers after Cavin1 (1–190) adsorption (Fig. 2*E*). The data showed significantly higher protein/lipid ratios for DOPC:DOPE:
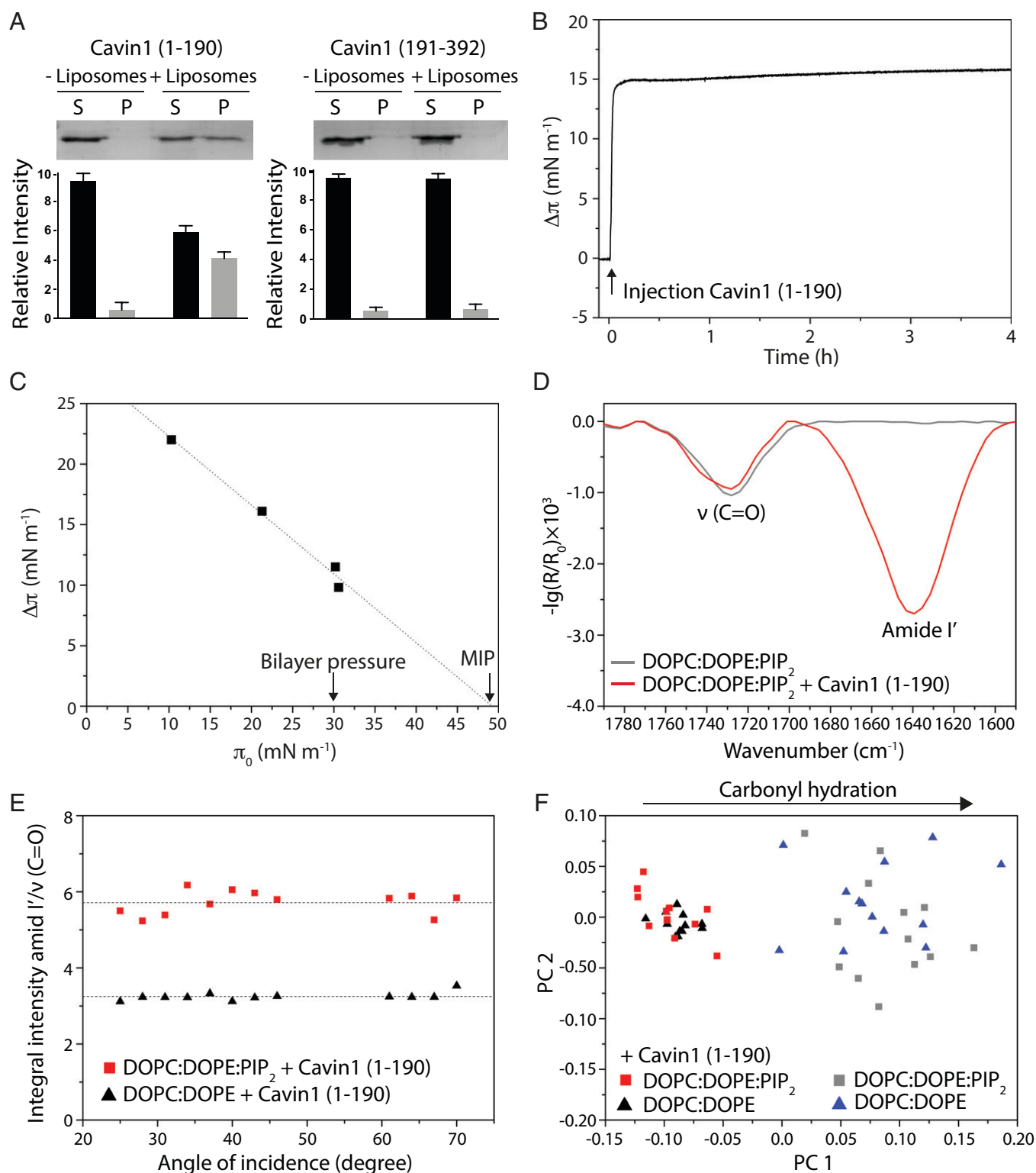
Fig. 2. Amount of Cavin1 (1–190) inserted into membranes is PI(4,5)P$_2$-dependent. (A) Liposome cosedimentation assay. Cavin1 (1–190) or Cavin1 (191–392) was incubated with or without liposomes and centrifuged, and supernatant and pellet fractions were analyzed by SDS-PAGE. Band intensities were quantified and data are shown as mean $\pm$ SEM (n = 3). (B) Cavin1 (1–190) adsorption to DOPC:DOPE:PI(4,5)P$_2$ monolayers. Cavin1 (1–190) was injected at π_0 = 20 mN·m^{-1} and $\Delta\pi$ was recorded over time. (C) Cavin1 (1–190) adsorption to lipid monolayers was measured at different π_0. MIP was determined by extrapolation of the $\Delta\pi/\pi_0$ plot to the x axis. (D) IRRA spectra (1,790 to 1,590 cm^{-1}) of DOPC:DOPE:PI(4,5)P$_2$ at π_0 = 20 mN·m^{-1}. The C=O vibrational band ($\sim$1,730 cm^{-1}) originates from lipid ester groups. The amide I' band ($\sim$1,640 cm^{-1}) indicates Cavin1 (1–190) adsorption after injection into the subphase. Spectra were acquired with p-polarized light at an angle of incidence of 40°. (E) Amount of protein adsorbed to the monolayer. Ratios of integral intensity of amide I' and C=O bands are shown as a function of the angles of incidence for the indicated lipid monolayers. Dotted lines display the mean of each dataset. (F) PCA in the C=O vibrational region based on IRRA spectra of DOPC:DOPE:PI(4,5)P$_2$ and DOPC:DOPE monolayers before and after adsorption of Cavin1 (1–190). PC1 represents the extent of carbonyl group hydration (76% of total variance), while PC2 (10%) showed no additional systematic changes.

PI(4,5)P$_2$ films [amide I′/ν(C=O) = 5.71 vs. 3.24, *$P < 0.05$], indicating a strong correlation between the presence of PI(4,5)P$_2$ and the amount of adsorbed Cavin1 (1–190). To study how insertion of Cavin1 (1–190) affects the lipid monolayer, we used the frequency of the carbonyl vibration, which is sensitive to H-bond formation and thus provides information on the lipid hydration at the hydrophilic–hydrophobic interface (25). Principal-component analysis (PCA) of a large number of recorded spectra revealed that the differences are indeed due to different extents of hydration (*SI Appendix*, Fig. S2D). Pure lipid monolayers displayed more hydrated carbonyls, and the binding of Cavin1 (1–190) resulted in less hydrated carbonyl groups (Fig. 2F). Moreover, IRRA spectra of pure lipid films at the surface pressure of injection (22 mN·m^{-1}) and after protein adsorption (36 mN·m^{-1}) (*SI Appendix*, Fig. S2F) were similar. This indicated that lipid dehydration is not an effect of increasing surface pressure following Cavin1 injection but can clearly be assigned to insertion of Cavin1 (1–190) into the lipid head group region and the concomitant replacement of hydration water.

HR1 Is Membrane-Bound in a Slightly Inclined Angle in the Presence of DR1 and DR2. To further address how membrane binding and insertion of Cavin1 (1–190) would affect the protein structure, we used far-UV (ultraviolet) circular dichroism (CD) spectroscopy. We found that Cavin1 (1–190) exhibited a predominantly α-helical CD profile with typical minima at 208 and 222 nm at both 300 and 150 mM NaCl (Fig. 3 A and B). However, following preincubation with liposomes, we noticed a dramatic change in the CD spectra at 150 mM NaCl but not at 300 mM NaCl (Fig. 3 A and B). This involved a significant increase of the ellipticity at 222 nm in relation to 208 nm (Fig. 3B), which is indicative of an increased hydrophobicity of the helix environment. This could derive from either membrane insertion or oligomerization, as both would protect the helical surfaces from the solvent. To further monitor how the HR1 domain, in combination with the DR1 and DR2 domains, would insert and orient at the membrane, we used IRRAS to get direct information on the secondary structure of the adsorbed protein and its orientation (20). The secondary structure of the protein is encoded in the position of the amide I′ band, whereas the orientation influences its intensity. Knowledge of the protein structure is essential for appropriate data analysis and determination of the orientation at the lipid monolayer. Since the crystal structure of HR1 (45–155) is known (15) and both DR1 (1–43) and DR2 (156–190) lack a secondary structure, we could use this technique to understand the membrane association of Cavin1 (1–190) in more detail. The asymmetric amide I′ band shape in the experimental spectra indeed indicated that in addition to helical structures, further components such as unordered structural elements were present (Fig. 3C). Moreover, the positions of the helical components are typical for a coiled-coil structure (26). This is in agreement with the combination of HR and DR domains (15). To predict the orientation of Cavin1 (1–190) when adsorbed to a DOPC:DOPE:PI(4,5)P$_2$ monolayer, experimental and simulated IRRA spectra recorded at various angles of incidence with parallel and perpendicularly polarized IR light were compared (Fig. 3C). The best fitting band simulation yielded an average inclination angle of $\gamma = 22.5 \pm 2.5°$ for the individual helical components of Cavin1 (1–190) with respect to the lipid monolayers (Fig. 3C). However, upon fitting simulated to experimental spectra at all theoretically possible inclination angles, we found that the minimum is rather shallow and spectral fits are reasonable for average helix inclination angles between 0° (parallel to the lipid layer; *SI Appendix*, Fig. S3A) and 30° (slightly inclined; Fig. 3D). Conversely, at higher inclination angles ($\gamma > 30°$), no acceptable spectral fit could be

obtained (*SI Appendix*, Fig. S3 B and C). It should be noted that an inclination angle of $\gamma = 0°$ could only be obtained if the HR1 helix bundle dissociates and all three helices adsorb individually and horizontally to the interface. If HR1 were to adsorb as an intact trimer, the smallest possible individual helix inclination angle would be $\gamma = 12°$ due to the intrinsic helix orientations within the bundle. Therefore, we also calculated the possible inclination angles of the intact trimer (Fig. 3D and *SI Appendix*, Fig. S3D). The minimum found in the IRRA spectral fit corresponds to a trimer inclination angle of 20 ± 3° (Fig. 3D). Our results implied that if the trimeric HR1 remained intact it would adsorb with a slight inclination to the interface, where average trimer inclination angles of 17 to 23° were most probable (Fig. 3D).

DR1 and DR2 Influence the Membrane-Binding Properties of HR1. To further examine the mechanism for how the N-terminal region (residues 1 to 190) interacts and inserts into the membrane, we generated and purified different truncated versions of the 1–190 region from *Escherichia coli* (Fig. 4A and *SI Appendix*, Fig. S4A). Using CD spectroscopy, we found that all constructs containing HR1 exhibited a predominantly α-helical CD profile in 300 mM NaCl buffer with typical minima at 208 and 222 nm (*SI Appendix*, Fig. S4B). However, at 150 mM NaCl concentration, the 44–190 construct lost the α-helical CD profile (*SI Appendix*, Fig. S4C). To analyze the oligomeric state of the constructs, we used mass photometry (Fig. 4B). All constructs were detected as trimers, although the measured molecular mass of all Cavin1 constructs was slightly higher than theoretically expected, likely due to the elongated structure of HR1 (Fig. 4B and *SI Appendix*, Fig. S4D). Notably, 1–190 was also detected as monomers, suggesting that DR1 and DR2 might destabilize HR1. Liposome cosedimentation analysis showed that 1–190, 44–155, 1–155, and 101–190 bound membranes, suggesting that the 101–155 region of HR1 is the minimal part of the protein required for adsorption (Fig. 4C). This region includes the positively charged patch of HR1, previously shown by mutational analysis to convey PI(4,5)P$_2$ binding (15). Notably, the 44–155 construct displayed more membrane binding as compared with constructs that contained DR1 and/or DR2 in addition to HR1 (Fig. 4D). To further assess this, we assayed the adsorption of Cavin1 (1–190), (1–155), (44–155), and (44–190) to SLBs using QCM-D. Interestingly, 1–155, 44–155, and 44–190 demonstrated much faster adsorption kinetics as well as a greater overall amount of protein adsorbed (−34.7 ± 1.2, −36.4 ± 1.5, and −31.0 ± 4.7 Hz, respectively) than was observed for 1–190 (−25.1 ± 3.4 Hz) (Fig. 4E). However, once the systems were rinsed with buffer, much faster desorption kinetics were also observed for 1–155, 44–155, and 44–190 in comparison with 1–190 (Fig. 4E). These data clearly show that the presence of DR1 and DR2 not only affects how HR1 initially binds to the membrane but also determines how strongly the protein is retained. This in turn could be tied to either the degree of membrane insertion or protein network formation. In order to better understand the impact of how these different regions lead Cavin1 to interact with the membrane, we calculated the softness of the adsorbed protein layer ($\Delta D/-\Delta F$) after rinsing and at equilibrium (Fig. 4F). The constructs without DR1 formed much stiffer/denser layers than constructs containing DR1. This observed difference in rigidity of the protein-coated membrane indicates that DR1 and DR2 greatly influence the binding of HR1 to the membrane and also affect the final conformation on the surface.

The Membrane Insertion Unit of HR1 Is Buried into Membranes. To study if the different truncated proteins would insert into membranes, their adsorption to monolayers was monitored. Injection of
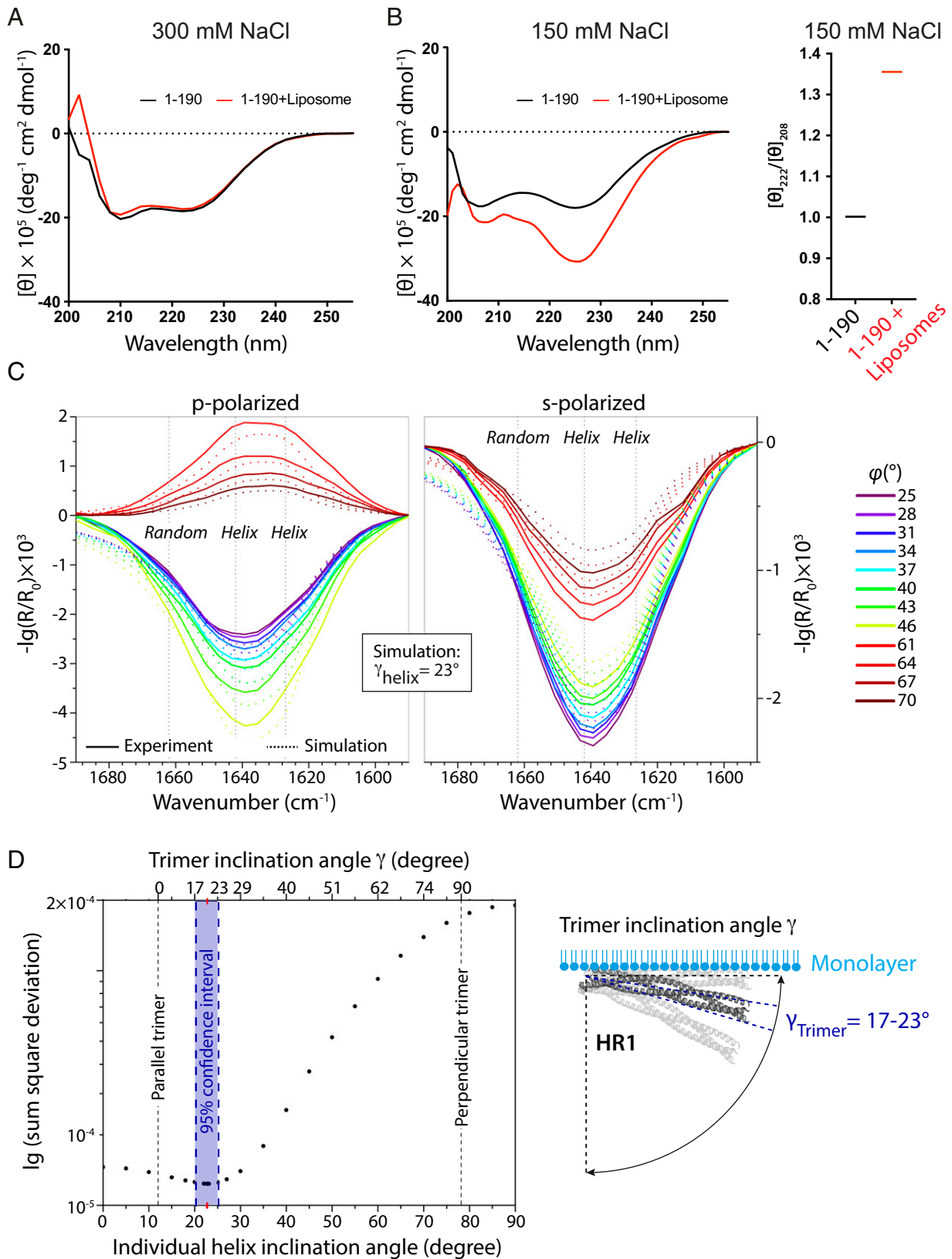
Fig. 3. Adsorption of Cavin1 (1–190) to membranes involves inclination of the helices in relation to the membrane. (*A* and *B*) Far-UV CD spectra (195 to 255 nm) of Cavin1 (1–190) with or without liposomes in 300 mM (*A*) or 150 mM (*B*) NaCl buffer. In *B*, the ratio between 222- and 208-nm ellipticities ($[\theta_{222}]/[\theta_{208}]$) in the absence and presence of liposomes is plotted (*Right*). (*C*) Experimental and best fitting simulated IRRA spectra of Cavin1 (1–190) adsorbed to a DOPC: DOPE:PI(4,5)P$_2$ monolayer, at various angles of incidence (φ) and polarizations. Vertical dotted lines indicate the band components used for simulation. The best fit was achieved with a helix inclination angle of $\gamma = 22.5 \pm 2.5°$ with respect to the lipid interface. (*D*) The quality of the fit was assessed as the sum square deviation between experimental and simulated spectra at various γ. The minimum is indicated by a red x-axis tick. The 95% CI of the minimum is shown in blue. The upper x axis shows the inclination angles of the complete HR1 trimer that correspond to the individual helices' inclination angles. Note that their relation is not linear. (*D, Right*) Scheme of the HR1 trimer orientation at the lipid monolayer. The most probable orientation is shown in dark gray and outlined by blue dotted lines.
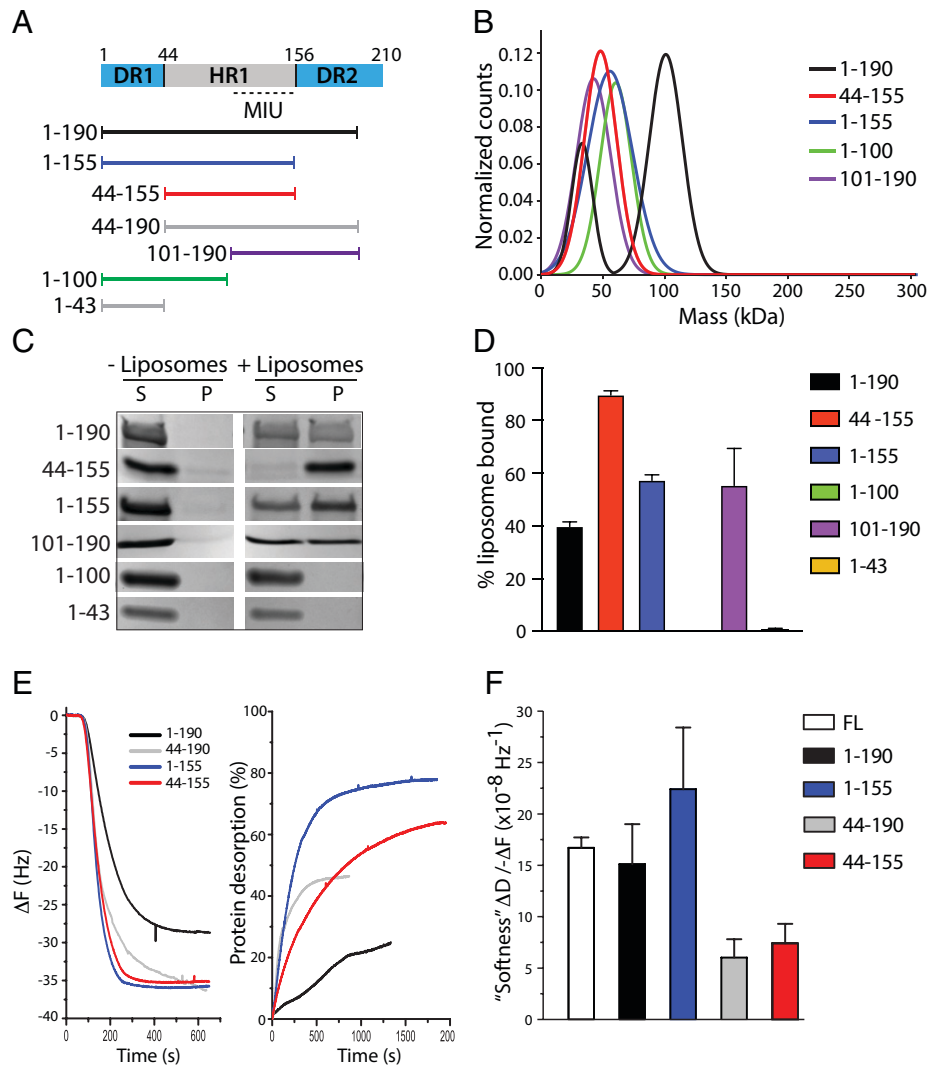
Fig. 4. DR1 and DR2 influence the membrane-binding properties of HR1. (*A*) Scheme of the Cavin1 N-terminal domains and purified protein constructs with defined amino acid numbers as indicated. (*B*) Gaussian fit of the molecular mass of Cavin1 constructs as determined using mass photometry. (*C*) Representative liposome cosedimentation of Cavin1 constructs as indicated. Proteins were incubated with or without DOPC:DOPE:PI(4,5)P$_2$ liposomes and centrifuged, and supernatant and pellet fractions were analyzed by SDS-PAGE. (*D*) Band intensities of the liposome cosedimentation assay were quantified and data are shown as mean ± SD (*n* = 3). (*E*) Frequency shift (Δ*F*, *Left*) as a result of adsorption of Cavin1 constructs onto SLBs measured by QCM-D. (*E*, *Right*) Extent of protein desorption following a rinse with 150 mM NaCl buffer. (*F*) Softness of the different adsorbed protein layers was calculated as (Δ*D*/−Δ*F*) after rinsing and at equilibrium. Data are shown as mean ± SD (*n* ≥ 2). FL, full-length.

Cavin1 (1–190), (1–155), and (101–190) resulted in an immediate steep increase in surface pressure (Fig. 5). These data suggested that residues 101 to 155 within the HR1 region, hereinafter referred to as the membrane insertion unit (MIU) (Fig. 4*A*), are responsible for insertion into membranes. Indeed, the MIP of residues 101 to 190 was similar to full-length Cavin1 (*SI Appendix*, Fig. S5*A*; 35.5 vs. 36.1 mN·m^{-1}, respectively). Interestingly, the 44–155 and 44–190 constructs, which both contain HR1 but lack DR1, resulted in a lower surface pressure increase and considerably lower rate of insertion (Fig. 5*A*). These data suggest DR1 significantly contributes to the ability of the MIU to insert into the monolayer in the presence of the entire HR1. DR1 (1–43) alone, or a 1:1 mixture of DR1 (1–43) and the HR1 (45–155) domain, resulted in a low surface pressure increase (*SI Appendix*, Fig. S5*B*), showing that a direct linkage between DR1 and/or DR2 with HR1 is required for efficient insertion.

Previous work has shown that removal of DR1 from full-length Cavin1 affected the ability of the protein to efficiently coassemble with CAV1 in cells (18). We could confirm these results showing that Cavin1-ΔDR1 only partially assembled together with CAV1

at the plasma membrane but that the majority of CAV1 was present in larger internal membranous structures, which were not detected in Cavin1-expressing cells (*SI Appendix*, Fig. S6 *A* and *B*). To address if this phenotype was due to defective membrane assembly, we purified the ΔDR1 (44–392) construct from mammalian cells and analyzed binding and insertion by QCM-D and monolayer adsorption experiments, respectively. We found that the ΔDR1 (44–392) construct appeared to bind slightly less to membranes (*SI Appendix*, Fig. S6*C*), and that the kinetics of membrane insertion was significantly affected (*SI Appendix*, Fig. S6*D*). However, at equilibrium, the MIP was similar to full-length Cavin1 (*SI Appendix*, Fig. S6*E*). This showed that also in the context of the full-length protein, DR1 influences the kinetics of membrane insertion and that the observed phenotype on caveolae assembly in cells is likely due to impaired membrane assembly and insertion.

Molecular Dynamics Analysis Reveals That Membrane Binding Triggers Partial Helical Separation of HR1 and Membrane Insertion of the MIU. The mechanism for membrane insertion of the MIU in the structural context of the trimeric HR1 is difficult to
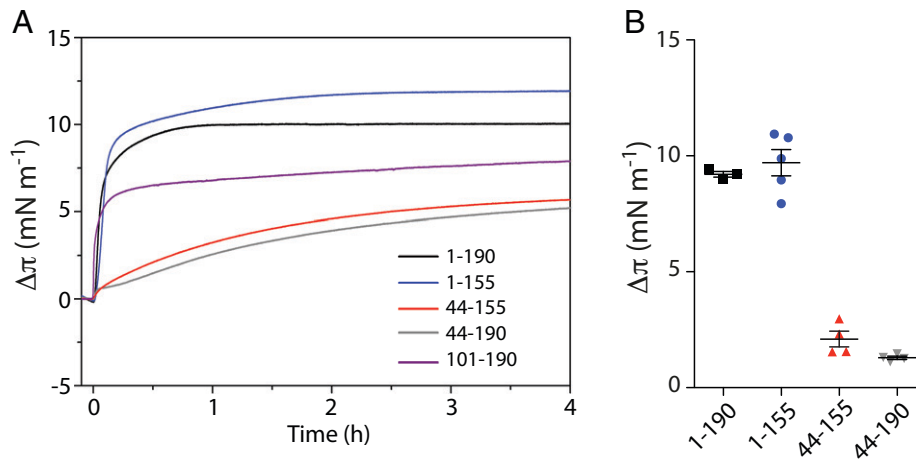
Fig. 5. MIU of HR1 is buried into membranes. (*A*) Adsorption of Cavin1 truncations as indicated to DOPC:DOPE:PI(4,5)P$_2$ monolayers. Proteins were injected at $\pi_0 = 20$ mN·m^{-1} and $\Delta\pi$ was recorded over time. (*B*) Quantification of $\Delta\pi$ recorded in *A* at $t = 20$ min. Data are shown as mean ± SEM.

envision. We therefore aimed to mechanistically dissect how the HR1 domain would bind and insert into membranes using molecular dynamics (MD) simulations. We limited the computational model to the HR1 domain, since the structure is described in detail, and it is the part of the protein known to interact with lipids. Using all-atom MD simulations, we found that the trimer bound to the membrane surface consisting of DOPC:DOPE:PI(4,5)P$_2$ upon first contact (Fig. 6*A*). Once bound, the protein remained in contact with the membrane for the entire course of the simulation. All three helices were engaged in hydrogen bonding once the trimer was horizontally attached and 56% of the bonds were formed between the trimer and PI(4,5)P$_2$ (Fig. 6 *B* and *C*). In particular, lysine residues in either the N- or C-terminal region of the HR1 domain contributed to most of the hydrogen-bonding interactions. Indeed, visualization of the solvent-inaccessible surface area confirmed that especially the termini of the trimer are in close contact with PI(4,5)P$_2$-rich regions of the membrane (Fig. 6*A*).

To address the temporal membrane binding of the HR1 domain, we performed coarse-grained MD (CG-MD) simulations. The HR1 domain was placed in a simulation box near lipid membranes composed of DOPC:DOPE, with or without PI(4,5)P$_2$, over a time frame of 2 μs. No binding was observed in the absence of PI(4,5)P$_2$ (*SI Appendix,* Fig. S7*A*) but, in its presence, lysine residues in either the N or C terminus of the HR1 domain initiated binding to this lipid (Fig. 7 *A, Top*). Subsequently, interactions between PI(4,5)P$_2$ and positively charged residues along the trimer surface resulted in a horizontal binding of HR1 in relation to the membrane in all simulations (Fig. 7 *A, Bottom* and Fig. 7 *B, Top*). In this state, HR1 was tightly packed toward the head group interphase. Interestingly, the individual helices facing the membrane appeared to be different in-between simulations (*SI Appendix,* Fig. S7*B*). In line with this, the positively charged residues interacting with PI(4,5)P$_2$ are distributed homogeneously around the surface of the rod-like HR1 domain (15). In our simulations, the average distance between the lipid head groups and the center of the bilayer was 1.95 nm (*SI Appendix,* Fig. S7*C*), in agreement with previous studies (27). The residues of HR1 closest to the membrane were on average 1.79 ± 0.15 nm from the bilayer center, suggesting that HR1 was shallowly buried in the membrane in-between the head groups (Fig. 7*C*). This could account for the intermediate increase in surface pressure detected for the HR1 domain in the monolayer experiments (Fig. 5*A*).

Interestingly, CG-MD also showed that the helices in HR1 could become slightly uncoiled (*SI Appendix,* Fig. S7*B*), suggesting that membrane interaction may induce partial separation of the helices in the HR1 trimer. To elucidate if the binding and insertion of HR1 involved separation of the coiled coil, we performed longer CG-MD simulations (36 μs). Interestingly, following the initial electrostatic interaction placing HR1 horizontally toward the membrane, the individual helices in the N or C terminus started to separate in all three 36-μs simulations (Fig. 7 *B, Bottom* and *SI Appendix,* Fig. S7*E*). Quantification of the number of helix–helix contacts in the trimer showed a consistent decrease over time in the presence of membranes (Fig. 7*D*). In comparison, no separation was observed in the absence of membranes (Fig. 7*D* and *SI Appendix,* Fig. S7*D*). Moreover, the membrane-induced separation resulted in further insertion of the helices into the membrane with a minimum average of 1.61 ± 0.26 nm from the bilayer center (Fig. 7 *B* and *C*), suggesting that membrane binding induces coiled-coil separation and insertion of Cavin1. Since helix separation was observed in both the N and C termini of HR1 in our simulations, we addressed the preferred membrane insertion orientation by simulating membrane binding of single-chain helices (Fig. 7*E*). We observed that the residues close to the C terminus of the individual helices were inserted into the membrane in all simulations. The residues closest to the membrane inserted below the head group region on average 1.51 ± 0.30 nm from the bilayer center (Fig. 7*C*). The observed insertion depth is less but in the same range as the previously described insertion of amphipathic helices (28). In one of these simulations, residues close to the N terminus were also inserted. This showed that uncoiling of the trimer would allow for the helices to insert deeper into the membrane as compared with the HR1 trimer. Taken together, we propose that HR1 initiates membrane binding of Cavin1 via electrostatic interactions with PI(4,5)P$_2$, resulting in tight packing toward the bilayer. This enables unwinding of the coiled coil and insertion of the MIU in-between the lipid head groups. Insertion is assisted by the repelling electrostatic nature of DR1 and DR2, which instead could mediate intermolecular interactions and Cavin1 networks, resulting in stable membrane insertion of Cavin1.

Discussion

The caveola coat has eluded detailed architectural description for decades but, based on structural analysis of both caveolae and the components building up the coat, different models have been
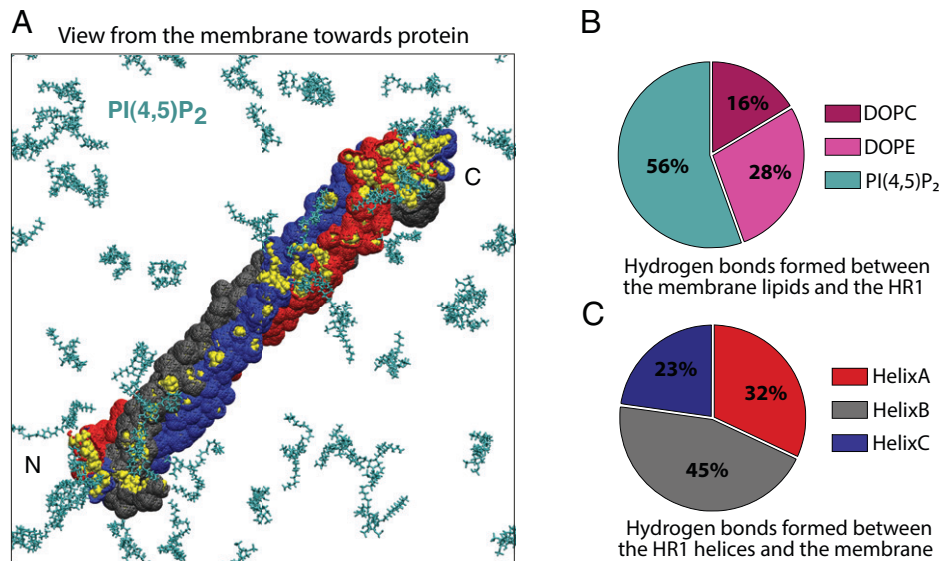
Fig. 6. HR1 domain binds via any of the three helices and orients parallel to the membrane interphase as revealed by MD analysis. (*A*) Representative bottom-up view from the membrane for all-atom simulations of HR1. Membranes consisted of DOPC, DOPE, and PI(4,5)P_2, but only PI(4,5)P_2 (turquoise) is shown for clarity. Residues highlighted in yellow were solvent-inaccessible and were partially engaged in hydrogen bonding with the membrane, predominantly with PI(4,5)P_2. (*B*) Pie chart showing the ratio of hydrogen bonding between the HR1 domain and lipids present in the membrane based on all-atom MD simulations. The data were analyzed over the last 200 ns of 300-ns simulations (three independent simulations). (*C*) Pie chart showing the ratio of hydrogen bonding between the membrane and individual helices of the trimer based on the all-atom MD simulation data.

proposed (13, 14, 29). Validation and further improvements of these models rely on detailed structural understanding of the individual protein components at the membrane interface. In this work, we have studied the initial binding and assembly of Cavin1 at the membrane interface. We found that Cavin1 inserted into the membrane via a mechanism dependent on the DR1–HR1–DR2–interacting unit. Hereby, HR1 undergoes dynamic transition from a shielded coiled-coil state in solution and a partially uncoiled state, where the MIU is partially buried in the membrane. Helix insertion has been shown to drive membrane curvature (30) but also to provide lipid specificity and targeting to specific cellular compartments, as in the case of proteins containing amphipathic lipid packing sensor motifs (31). The described membrane insertion of Cavin1 would allow it to directly interact with lipid acyl chains. Such interactions could be linked to the recently reported lipid-sorting activity of the caveola coat, which was shown to be sensitive to the saturation level of acyl chains (6). The proposed mechanistic steps could provide specificity and regulation to the assembly process and enable Cavin1 to generate membrane curvature and interact with the integral part of CAV1 below the head group region of the membrane.

To characterize the properties of Cavin1 membrane binding in detail, we used purified full-length and truncated versions of Cavin1 in combination with different membrane model systems. Thereby, we have been able to reconstitute and measure membrane binding and insertion of Cavin1 using a variety of biophysical techniques. The presented membrane insertion mechanism of Cavin1 was supported by the salt-resistant binding of Cavin1 to SLBs as measured in real time using QCM-D. Furthermore, the IRRAS analysis showed that membrane binding of Cavin1 is coupled to decreased hydration of the lipid carbonyl groups, suggesting that Cavin1 inserted below the head group region of the membrane. Direct evidence for this comes from surface pressure measurements using Langmuir lipid monolayers, which showed that Cavin1 rapidly inserts into lipid monolayers containing PI(4,5)P_2. This was indicated by a steep increase in surface pressure, showing that the protein inserted in-between the head groups of the lipids. The MIP of Cavin1 was higher than the

monolayer–bilayer equivalence pressure, suggesting that Cavin1 spontaneously inserts into cellular membranes. The MIP is furthermore very similar to other proteins shown to insert into membranes using this methodology, such as the BAR domain of Bin1 (32) and Sar1p (33). Using analysis of truncated protein constructs, we mapped the MIU to the C-terminal part of HR1, which contains hydrophobic and positively charged residues key to membrane binding.

Using a combination of CG and all-atom MD simulations, we were able to dissect the binding interface of HR1 and the hydrogen bonds formed with PI(4,5)P_2. We found that binding was initiated and further supported by electrostatic interactions between PI(4,5)P_2 and lysine residues along HR1 resulting in tight horizontal docking of the HR1 domain. This is similar to previous simulations with a different lipid composition, POPC: POPS:PI(4,5)P_2 (80:15:5 mol%) (6). Interestingly, we found that different helices of the trimeric HR1 were facing the membrane in the individual simulations. This is in agreement with the fact that the positively charged residues are distributed homogeneously around the surface of the rod-like HR1 trimer. This is dissimilar from other membrane-binding domains, such as BAR domains, indicating that HR1-mediated membrane association of Cavin1 uses another type of mechanism.

Cavin1 has been proposed to bind as rod-like trimers based on the current structural knowledge. Yet the striations detected on the caveolae bulb have been difficult to correlate to such Cavin1 rods, suggesting that the structure of Cavin1 might be flexible and change upon membrane association. Using CD spectroscopy, we observed that membrane binding of Cavin1 induced structural rearrangements in HR1, and IRRAS analysis revealed that the inclination angle of membrane-bound HR1 was slightly tilted. Furthermore, when CG simulations of HR1 were performed for an extended time, we observed that the helices interacting with the membrane separated, which allowed the MIU to insert deeper in-between the head groups. Indeed, the individual helices of HR1 were able to insert deeper into the membrane as compared with the trimer. Taken together, these results support the idea that the HR1 trimer partially uncoils to
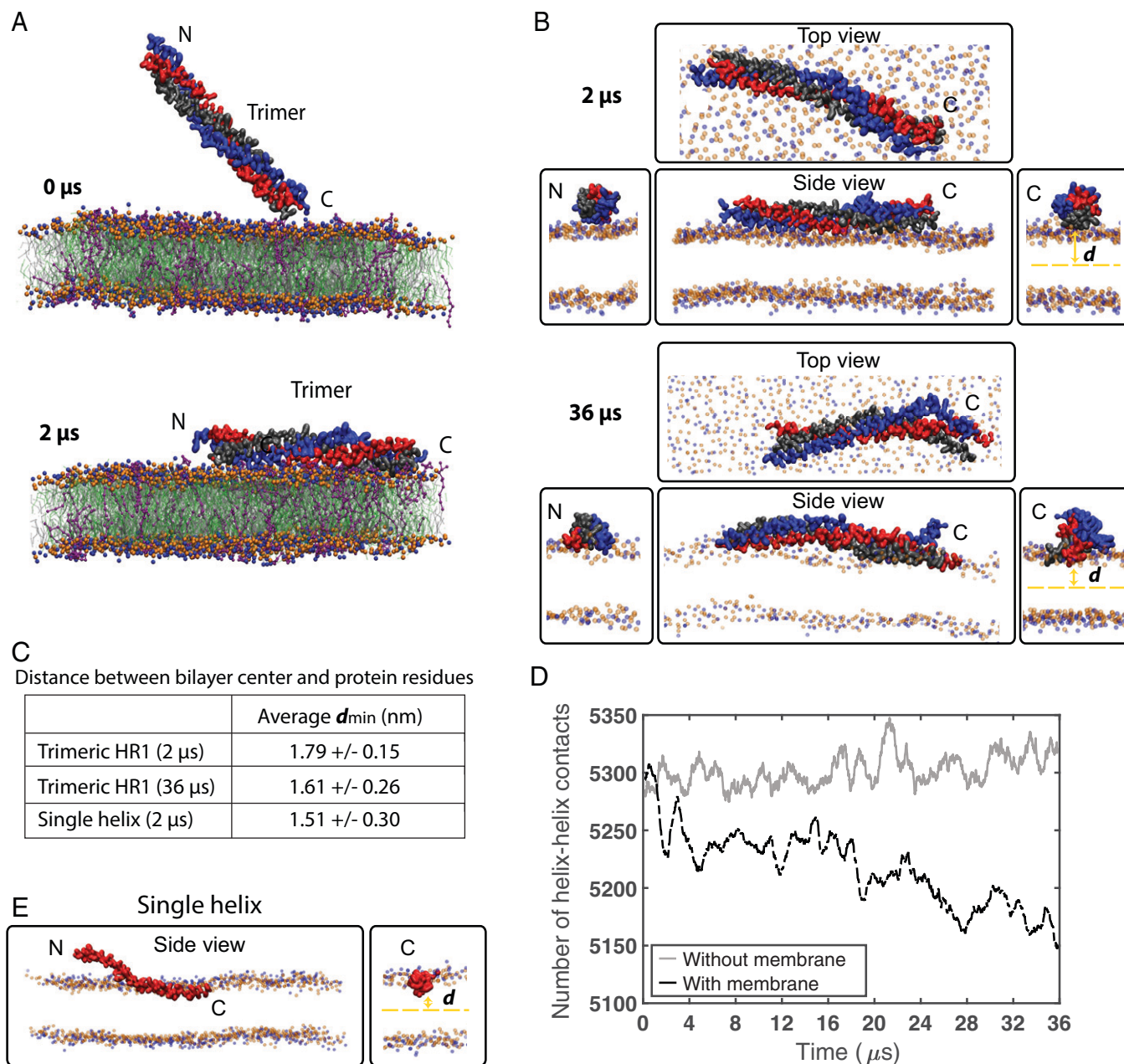
Fig. 7. MD analysis shows that partial helix separation facilitates insertion of the MIU. (*A*) CG-MD simulations (0 to 2 μs) of HR1 membrane binding. Helices A, B, and C are color-coded as blue, red, and gray, respectively. Membranes consisted of DOPC (silver), DOPE (green), and PI(4,5)P$_2$ (purple), where head group beads are shown in blue and orange. Binding was initiated by the N or C terminus (*Top*; see also *SI Appendix*, Fig. S7B for other simulations) and HR1 was horizontally bound at the end of all simulations (*Bottom*). (*B*) Snapshots of the protein–membrane interaction from different viewing angles shown at 2 and 36 μs (*Top* and *Bottom*, respectively). Water and membrane tail beads are omitted for clear representation. "*d*" indicates the minimum distance from the membrane center to the protein surface. (*C*) Overview of the average minimum distances *d* between the bilayer center and the protein residues as determined in MD simulations over time and shown as averaged between the last 500 ns for the 2-μs-long simulations and 34 μs for the 36-μs-long simulations. Data are shown as mean ± SD (*n* ≥ 3). (*D*) Quantification of the number of helix–helix contacts within protein trimers over time in the presence or absence of lipid membrane. (*E*) Representative snapshot of CG-MD simulations (2 μs) from different viewing angles as in *B* of the monomeric HR1 domain (red) inserted into the membrane.

expose hydrophobic residues, hidden inside the coiled core, during membrane binding and insertion. Helical uncoiling could be driven by the interactions between PI(4,5)P$_2$ head groups and the individual helices in a rotational movement competing with the interactions stabilizing the coiled coil. Similar drastic conformational changes have been observed in other proteins upon membrane binding, for example, membrane-driven exposure of amphipathic helices in small G proteins (30) and the major helical rearrangement in the pore-forming proteins Bak and Bax upon membrane binding (34).

Our Langmuir trough data showed that membrane binding of HR1 alone was inefficient in mediating membrane insertion. Instead, this was dependent on combining HR1 with flanking disordered regions, suggesting that the interplay between the negatively charged DR1 and DR2 and the positively charged HR1 is important. Indeed, QCM-D data comparing combinations of HR1 with DR1 and/or DR2 showed that the softness of the membrane was dramatically altered in comparison with the full-length Cavin1, unless all three regions were present. Indeed, deletion of DR1 in the full-length protein affected the kinetics of membrane

insertion and assembly of caveolae in cells, in agreement with previous reports (18). We propose that DR1 and DR2 contribute to the destabilization of the HR1 coiled coil, thereby promoting insertion of the MIU.

This is consistent with these regions being important for intermolecular interactions and Cavin1 network formation (13). In line with this, DR1 was shown to be required for Cavin1-induced membrane remodeling of spherical liposomes into membrane tubules. The disordered regions were proposed to influence assembly of Cavin1 via "fuzzy" electrostatic interactions with the helical regions. This induces a liquid–liquid phase separation and contributes to molecular crowding, which was proposed to drive membrane curvature and generate a metastable caveola coat (18). Our in vitro and in silico data are consistent with this model and extend the implications of the weak electrostatic interactions between DR1, DR2, and HR1 to membrane insertion. Taken together, the dynamic membrane insertion mechanism of Cavin1 described here provides a mechanistic basis for membrane-assisted regulation of caveola coat assembly.

Materials and Methods

Lipids. POPC (1-palmitoyl-2-oleoyl-*sn*-glycero-3-phosphocholine), PI(4,5)P$_2$ (L-α-phosphatidylinositol-4,5-bisphosphate, porcine brain, ammonium salt), DOPC (1,2-dioleoyl-*sn*-glycero-3-phosphocholine), DOPE (1,2-dioleoyl-*sn*-glycero-3-phosphoethanolamine), and brain total lipid extract (FOLCH fraction, porcine) were purchased as lyophilized powder from Avanti Polar Lipids.

Protein Purification. Cavin1 truncation protein residues 1 to 43, 44 to 155, 44 to 190, 1 to 155, 1 to 190, 1 to 100, 101 to 190, and 191 to 392 were purified as described previously (16). Proteins were expressed with N-terminal 6×His tags in *E. coli* Rosetta pLysS or BL21(DE3)pLysS (growth in Terrific Broth media). Protein expression was induced with 1.0 mM isopropyl β-D-1-thiogalactopyranoside at the exponential phase and incubated overnight at 20 °C. TALON Superflow (Cytiva) was used for affinity purification. Imidazole was removed by gel filtration chromatography using Sephacryl S-300 HR (Bio-Rad). Full-length Cavin1 and ΔDR1 mutants were expressed and purified from suspension cells HEK-293F (Invitrogen) as described previously (35). Cells were grown to 2 to 3 × 10^6 cells per milliliter on a shaker (160 rpm) at 37 °C with 8% CO$_2$ in 4 mM glutamine-supplemented BalanCD medium (Irvine Scientific). A total of 1 µg per 10^6 cells of the plasmids containing the cytomegalovirus promoter and 3×FLAG-tagged genes was mixed with a threefold excess (weight/weight) of polyethylenimine MAX 40 kDa (Polysciences) in 4 mL OptiPRO (Invitrogen). The mixture was incubated for 20 min at room temperature before being added to the cell cultures. Cells were grown for 2 d with an addition of 5% BalanCD Feed (Irvine Scientific) per day. Cells were harvested, and lysed with 1% Nonidet P-40 (Thermo Fisher Scientific) for 15 min on ice. Following centrifugation at 20,000 × *g* for 10 min, the supernatant was added to 3 mL anti-Flag (M2) agarose (Sigma), and incubated at 4 °C overnight. The gel matrix was transferred to a column and washed with 10 column volumes of 20 mM Hepes, 300 mM NaCl (pH 7.4). In order to remove Hsp70 chaperones, the matrix was incubated with a buffer containing 5 mM adenosine triphosphate, 20 mM MgCl$_2$, 10 mM KCl, and 0.1% Nonidet P-40 for 2 h. The protein was eluted with 100 µg/mL 3×FLAG peptide (Sigma). The eluted protein was adjusted to the desired concentration via Vivaspin (Sartorius), analyzed by sodium dodecyl sulfate–polyacrylamide gel electrophoresis (SDS-PAGE), snap-frozen in liquid nitrogen, and stored at −80 °C.

Liposome Cosedimentation Assay. The liposome cosedimentation assay was performed as previously described (36). Briefly, FOLCH lipids or formulated lipid mixtures composed of DOPC:DOPE:PI(4,5)P$_2$ (55:45:5 mol%) were dissolved to a final concentration of 1 mg/mL in chloroform:methanol (3:1 volume/volume; vol/vol). Lipids were dried under a stream of nitrogen and rehydrated in 20 mM Hepes buffer, 150 mM NaCl (pH 7.4) followed by bath sonication (Transsonic T310, Elma Schmidbauer). Proteins were incubated with liposomes at a final concentration of 3 µM and 0.5 mg/mL, respectively, for 15 min at room temperature. The samples were centrifuged at 100,000 × *g* for 20 min at room

temperature. Then, the supernatant and pellet were analyzed by Coomassie-stained SDS-PAGE, and quantified using Image Lab software (Bio-Rad).

SLBs and QCM-D. Vesicles for forming SLBs were prepared as described in *Liposome Cosedimentation Assay*, except for the vesicles containing POPC:PI(4,5)P$_2$ (95:5 mol%), which were extruded 11 times (Mini Extruder, Avanti) through a polycarbonate filter (Nuclepore Track-Etched Membranes, Whatman) with 100-nm pore size. An X4 unit (AWSensors) equipped with a flow chamber was used to conduct the QCM-D measurements. Wrapped 14-mm (5 MHz, Cr/Au–SiO$_2$, polished) sensors were used for all experiments. Each sensor was stored in 2% SDS overnight and treated with UV/ozone (BioForce Nanosciences) for 30 min prior to use. The frequency and dissipation changes for overtones 1, 3, 5, 7, 9, and 11 were all recorded, but only the third overtone is reported herein. POPC:PI(4,5)P$_2$ vesicles (100 µL, 0.1 mg/mL) in 20 mM citrate, 50 mM KCl, 0.1 mM ethylenediaminetetraacetate (pH 4.5) were injected in a continuous flow and SLB formation was monitored. After SLB formation, the chambers were rinsed with buffer (20 mM Hepes, 150 mM NaCl, pH 7.4). After reaching a stable baseline, protein was injected into the chamber. Flow was paused once the protein solution had filled the sensor chamber and the system was allowed to reach equilibrium before rinsing with the buffer. High-salt treatment was done by rinsing the sensor surface with the same buffer but a higher salt concentration (300 mM NaCl) followed by rinsing with the initial buffer (150 mM NaCl).

Lipid Monolayer Experiments. Lipid monolayer experiments were performed with either a custom-built round PTFE trough at Martin Luther University Halle-Wittenberg (Ø 60 × 3 mm, Riegler and Kirstein) or a Microtrough G1 System at Umeå University (Ø 53 × 4 mm, Kibron). Both troughs were covered to prevent temperature and humidity loss and the temperature of the subphase was controlled through a circulating water bath. Lipid mixtures consisting of DOPC:DOPE:PI(4,5)P$_2$ (55:45:5 mol%) were prepared at a total lipid concentration of 1 mM in chloroform:methanol (3:1 vol/vol). A microbalance equipped with a Wilhelmy plate was used to measure the surface pressure (π) and calibrated before each measurement. Lipid solutions were deposited onto the surface of the subphase (25 mM Hepes, 300 mM NaCl, 25 mM KOH, pH 7.4) to obtain the required initial surface pressure (π$_0$). The subphase was continuously stirred by a magnetic stirrer. After the solvent had been allowed to evaporate for 15 min and a stable monolayer was formed, the protein was injected under the lipid film directly into the subphase using a thin syringe needle (final concentration 50 nM). Curve analysis of the Δπ/π$_0$ plot provides the synergy factor (*a*) as the slope of the linear regression +1. A positive *a* is indicative for attractive interactions between the lipid monolayer and the injected protein, while *a* = 0 would indicate a lack of interactions. The MIP was determined from the Δπ/π$_0$ plot through linear extrapolation to the *x* axis, namely it corresponds to π$_0$ at Δπ = 0 (22). The SD of the MIP value was calculated according to the formula given in ref. 22. Analysis of the adsorption curves was performed with Origin 8.1 (OriginLab).

Monolayer Measurements with IRRAS. The Langmuir trough system used in combination with IRRAS (Riegler and Kirstein) included a circular sample (Ø 60 mm, 7.4 mL) and a rectangular reference trough (30 × 6 cm). The levels of the subphase (either H$_2$O- or D$_2$O-based) were controlled with a built-in laser and could be externally regulated via a pump system. The subphase was maintained at 20 °C through a circulating water bath. The same procedure as above was followed for preparation of the lipid film. IRRAS experiments were conducted with a Bruker Vertex 70 Fourier-transform IR spectrometer equipped with an A 511 reflection unit (Bruker) and an external mercury cadmium telluride detector. The entire setup was enclosed and purged to keep the relative humidity constant. IRRA spectra of the films were acquired at various angles of incidence (between 25 and 70°) using parallel (p) and perpendicularly (s) polarized IR light; 2,000 scans were accumulated in p and 1,000 were accumulated in s polarization of the IR beam with a resolution of 8 cm^{-1} and a scanner frequency of 80 kHz. An additional zero filling factor of 2 was applied to the averaged interferograms prior to Fourier transformation. The single-beam reflectance spectra of the reference (R_0) and the sample (R) trough surfaces were used to calculate the reflection–absorption spectrum as lg(R/R_0). Details for IRRAS simulation, band-fitting parameters, and PCA are described in *SI Appendix*.

CD Spectroscopy. The secondary structure of cavins was analyzed using a CD spectropolarimeter (JASCO, J-810) at 25 °C in the presence and absence of

FOLCH liposomes. The final protein and liposome concentration was 3 μM and 0.5 mg/mL, respectively, in 25 mM Hepes, 150 mM NaCl (pH 7.4). A cuvette with a 0.1-cm path length was used to acquire the spectra, which were measured from 190 to 260 nm by averaging eight scans of each sample at a bandwidth of 2 nm and a scan rate of 50 nm/min. All samples were incubated for 5 min until equilibrium temperatures were reached. Buffer- and liposome-only spectra were measured as background signals that were subtracted from protein signal.

Mass Photometry. Mass and oligomerization measurements were performed on glass coverslips (no. 1.5 H, 24 × 50 mm, Marienfeld) with a CultureWell reusable gasket (Grace Bio-Labs) placed on top and recorded on a mass photometer (Two^{MP}, Refeyn). The gasket well was filled with the sample (25 to 100 nM) and data acquisition was performed using AcquireMP (Refeyn) for 60 s. Each measurement was repeated at least three times. The recorded videos were analyzed using DiscoverMP (Refeyn) where the data were processed and fitted with Gaussian function. The molecular mass was obtained by contrast comparison with bovine serum albumin standard calibrants measured on the same day.

Computational Simulations. All simulations were performed using GRO-MACS 2018 software (37), and the mouse Cavin1 HR1 domain structure (PDB ID code 4QKV) was used as the initial model (15). The membrane binding and insertion of the HR1 domain, including trimer orientation and rotation, were predicted using CG-MD simulations. The hydrogen bonds and HR1 domain–membrane interactions were predicted by all-atom MD simulations. Details for software, scripts, and parameters are described in *SI Appendix*.

Cell Culture, Transfection, and Live-Cell Microscopy. PC-3 cells (ECACC 90112714) were maintained in RPMI medium (GIBCO, Thermo Fisher Scientific) supplemented with 10% fetal bovine serum and penicillin/streptomycin. For live-cell confocal imaging, 400,000 cells were seeded on 1.5 high-tolerance 25-mm glass coverslips (Warner Instruments) 24 h prior to transfection. Caveolin1–red fluorescent protein, Cavin1–green fluorescent protein (GFP), and Cavin1-ΔDR1-GFP were transiently transfected using Lipofectamine 3000 (Invitrogen) according to the manufacturer's instructions 16 to 24 h before the experiment. Live-cell experiments were performed using a growth chamber (37 °C, 5% CO$_2$) connected to an Eclipse Ti-E inverted microscope (Nikon Instruments) equipped with a DU897 ANDOR electron multiplying charge-coupled device camera (Oxford Instruments), Nikon CFI Plan Apochromat 60× oil (numerical aperture [NA] 1.40) differential interference contrast objective, and Nikon CFI Plan Apochromat 100× (NA 1.49). The total internal reflection fluorescence objective was controlled by an NIS Elements interface (Nikon Instruments). Images were prepared using ImageJ (38) and Photoshop CS6 (Adobe).

1. R. G. Parton, M. M. Kozlov, N. Ariotti, Caveolae and lipid sorting: Shaping the cellular response to stress. *J. Cell Biol.* **219**, e201905071 (2020).
2. R. G. Parton, K.-A. McMahon, Y. Wu, Caveolae: Formation, dynamics, and function. *Curr. Opin. Cell Biol.* **65**, 8–16 (2020).
3. R. G. Parton et al., Caveolae: The FAQs. *Traffic* **21**, 181–185 (2020).
4. M. Hubert et al., Lipid accumulation controls the balance between surface connection and scission of caveolae. *eLife* **9**, e55038 (2020).
5. A. Fujita, J. Cheng, K. Tauchi-Sato, T. Takenawa, T. Fujimoto, A distinct pool of phosphatidylinositol 4,5-bisphosphate in caveolae revealed by a nanoscale labeling technique. *Proc. Natl. Acad. Sci. U.S.A.* **106**, 9256–9261 (2009).
6. Y. Zhou et al., Caveolin-1 and cavin act synergistically to generate a unique lipid environment in caveolae. *J. Cell Biol.* **220**, e202005138 (2021).
7. M. Hubert, E. Larsson, R. Lundmark, Keeping in touch with the membrane; protein- and lipid-mediated confinement of caveolae to the cell surface. *Biochem. Soc. Trans.* **48**, 155–163 (2020).
8. A. Ludwig et al., Molecular composition and ultrastructure of the caveolar coat complex. *PLoS Biol.* **11**, e1001640 (2013).
9. Y. Gambin et al., Single-molecule analysis reveals self assembly and nanoscale segregation of two distinct cavin subcomplexes on caveolae. *eLife* **3**, e01434 (2013).
10. K. G. Rothberg et al., Caveolin, a protein component of caveolae membrane coats. *Cell* **68**, 673–682 (1992).
11. A. R. Busija, H. H. Patel, P. A. Insel, Caveolins and cavins in the trafficking, maturation, and degradation of caveolae: Implications for cell physiology. *Am. J. Physiol. Cell Physiol.* **312**, C459–C477 (2017).
12. M. M. Hill et al., PTRF-cavin, a conserved cytoplasmic protein required for caveola formation and function. *Cell* **132**, 113–124 (2008).
13. M. Stoeber et al., Model for the architecture of caveolae based on a flexible, net-like assembly of Cavin1 and caveolin discs. *Proc. Natl. Acad. Sci. U.S.A.* **113**, E8069–E8078 (2016).
14. A. Ludwig, B. J. Nichols, S. Sandin, Architecture of the caveolar coat complex. *J. Cell Sci.* **129**, 3077–3083 (2016).
15. O. Kovtun et al., Structural insights into the organization of the cavin membrane coat complex. *Dev. Cell* **31**, 405–419 (2014).
16. J. Mohan, B. Morén, E. Larsson, M. R. Holst, R. Lundmark, Cavin3 interacts with cavin1 and caveolin1 to increase surface dynamics of caveolae. *J. Cell Sci.* **128**, 979–991 (2015).
17. V. A. Tillu et al., A variable undecad repeat domain in cavin1 regulates caveola formation and stability. *EMBO Rep.* **19**, e45775 (2018).
18. V. A. Tillu et al., Cavin1 intrinsically disordered domains are essential for fuzzy electrostatic interactions and caveola formation. *Nat. Commun.* **12**, 931 (2021).
19. N.-J. Cho, C. W. Frank, B. Kasemo, F. Höök, Quartz crystal microbalance with dissipation monitoring of supported lipid bilayers on various substrates. *Nat. Protoc.* **5**, 1096–1106 (2010).
20. A. Blume, A. Kerth, Peptide and protein binding to lipid monolayers studied by FT-IRRA spectroscopy. *Biochim. Biophys. Acta* **1828**, 2294–2305 (2013).
21. É. Boisselier, P. Calvez, É. Demers, L. Cantin, C. Salesse, Influence of the physical state of phospholipid monolayers on protein binding. *Langmuir* **28**, 9680–9688 (2012).
22. P. Calvez, S. Bussières, É. Demers, C. Salesse, Parameters modulating the maximum insertion pressure of proteins and peptides in lipid monolayers. *Biochimie* **91**, 718–733 (2009).
23. A. Blume, A comparative study of the phase transitions of phospholipid bilayers and monolayers. *Biochim. Biophys. Acta* **557**, 32–44 (1979).
24. D. Marsh, Lateral pressure in membranes. *Biochim. Biophys. Acta* **1286**, 183–223 (1996).
25. A. Blume, W. Hübner, G. Messner, Fourier transform infrared spectroscopy of ^{13}C=O-labeled phospholipids hydrogen bonding to carbonyl groups. *Biochemistry* **27**, 8239–8249 (1988).
26. M. Rabe, C. Schwieger, H. R. Zope, F. Versluis, A. Kros, Membrane interactions of fusogenic coiled-coil peptides: Implications for lipopeptide mediated vesicle fusion. *Langmuir* **30**, 7724–7735 (2014).
27. W. Ding, M. Palaiokostas, W. Wang, M. Orsi, Effects of lipid composition on bilayer membranes quantified by all-atom molecular dynamics. *J. Phys. Chem. B* **119**, 15263–15274 (2015).
28. M. A. Zhukovsky, A. Filograna, A. Luini, D. Corda, C. Valente, Protein amphipathic helix insertion: A mechanism to induce membrane fission. *Front. Cell Dev. Biol.* **7**, 291 (2019).
29. R. G. Parton, V. Tillu, K.-A. McMahon, B. M. Collins, Key phases in the formation of caveolae. *Curr. Opin. Cell Biol.* **71**, 7–14 (2021).
30. M. Giménez-Andrés, A. Čopič, B. Antonny, The many faces of amphipathic helices. *Biomolecules* **8**, 45 (2018).
31. S. Vanni et al., Amphipathic lipid packing sensor motifs: Probing bilayer defects with hydrophobic residues. *Biophys. J.* **104**, 575–584 (2013).
32. A. Auerswald, T. Gruber, J. Balbach, A. Meister, Lipid-dependent interaction of human N-BAR domain proteins with sarcolemma mono- and bilayers. *Langmuir* **36**, 8695–8704 (2020).
33. C. Schwieger, A. Meister, S. Daum, A. Blume, K. Bacia, Binding of the GTPase Sar1 to a lipid membrane monolayer: Insertion and orientation studied by infrared reflection–absorption spectroscopy. *Polymers (Basel)* **9**, 612 (2017).
34. D. Westphal, R. M. Kluck, G. Dewson, Building blocks of the apoptotic pore: How Bax and Bak are activated and oligomerize during apoptosis. *Cell Death Differ.* **21**, 196–205 (2014).
35. A. H. Lystad et al., Distinct functions of ATG16L1 isoforms in membrane binding and LC3B lipidation in autophagy-related processes. *Nat. Cell Biol.* **21**, 372–383 (2019).
36. E. Larsson, M. Hubert, R. Lundmark, "Analysis of protein and lipid interactions using liposome co-sedimentation assays" in *Caveolae: Methods and Protocols*, C. M. Blouin, Ed. (Springer US, New York, NY, 2020), pp. 119–127.
37. M. J. Abraham et al., GROMACS: High performance molecular simulations through multi-level parallelism from laptops to supercomputers. *SoftwareX* **1–2**, 19–25 (2015).
38. J. Schindelin et al., Fiji: An open-source platform for biological-image analysis. *Nat. Methods* **9**, 676–682 (2012).